ORIGINAL ARTICLE

Left ventricle diastolic vortex ring characterization in ischemic cardiomyopathy: insight into atrio-ventricular interplay

Alessandra Riva[1,2] · Simone Saitta[2] · Francesco Sturla[1,2] · Giandomenico Disabato[3] · Lara Tondi[3,4] · Antonia Camporeale[3] · Daniel Giese[5] · Serenella Castelvecchio[6] · Lorenzo Menicanti[6] · Alberto Redaelli[2] · Massimo Lombardi[3] · Emiliano Votta[1,2]

Abstract

Diastolic vortex ring (VR) plays a key role in the blood-pumping function exerted by the left ventricle (LV), with altered VR structures being associated with LV dysfunction. Herein, we sought to characterize the VR diastolic alterations in ischemic cardiomyopathy (ICM) patients with systo-diastolic LV dysfunction, as compared to healthy controls, in order to provide a more comprehensive understanding of LV diastolic function. 4D Flow MRI data were acquired in ICM patients ($n = 15$) and healthy controls ($n = 15$). The λ_2 method was used to extract VRs during early and late diastolic filling. Geometrical VR features, e.g., circularity index (CI), orientation (α), and inclination with respect to the LV outflow tract (β), were extracted. Kinetic energy (KE), rate of viscous energy loss ($\dot{EL}$), vorticity (W), and volume (V) were computed for each VR; the ratios with the respective quantities computed for the entire LV were derived. At peak E-wave, the VR was less circular ($p = 0.032$), formed a smaller α with the LV long-axis ($p = 0.003$) and a greater β ($p = 0.002$) in ICM patients as compared to controls. At peak A-wave, CI was significantly increased ($p = 0.034$), while α was significantly smaller ($p = 0.016$) and β was significantly increased ($p = 0.036$) in ICM as compared to controls. At both peak E-wave and peak A-wave, $\dot{EL}_{VR}/\dot{EL}_{LV}$, W_{VR}/W_{LV}, and V_{VR}/V_{LV} significantly decreased in ICM patients vs. healthy controls. KE_{VR}/V_{VR} showed a significant decrease in ICM patients with respect to controls at peak E-wave, while V_{VR} remained comparable between normal and pathologic conditions. In the analyzed ICM patients, the diastolic VRs showed alterations in terms of geometry and energetics. These derangements might be attributed to both structural and functional alterations affecting the infarcted wall region and the remote myocardium.

Keywords 4D Flow MRI · Ischemic cardiomyopathy · Left ventricle · Vortex quantification · Cardiac magnetic resonance · lambda2

Abbreviations

4D Flow MRI	time-resolved phase-contrast MRI with three-directional velocity encoding
bSSFP	balanced steady-state free precession
CI	Circularity Index
DSI	Diastolic Sphericity Index
EDV	End-Diastolic Volume
EF	Ejection Fraction
$\dot{EL}$	Rate of viscous energy loss
ESV	End-Systolic Volume
ICM	Ischemic Cardiomyopathy
KE	Kinetic Energy
LA	Left Atrium
LGE	Late Gadolinium Enhancement
LV	Left Ventricle
LVGFI	Left Ventricle Global Functionality Index
MRI	Magnetic Resonance Imaging

✉ Francesco Sturla
francesco.sturla@grupposandonato.it

1 3D and Computer Simulation Laboratory, IRCCS, Policlinico San Donato, Piazza E. Malan 2, San Donato Milanese, Italy

2 Department of Electronics, Information and Bioengineering, Politecnico Di Milano, Milan, Italy

3 Multimodality Cardiac Imaging, IRCCS Policlinico San Donato, San Donato Milanese, Italy

4 Department of Radiology, IRCCS Foundation Ca' Granda Ospedale Maggiore Policlinico, University of Milan, Milan, Italy

5 Magnetic Resonance, Siemens Healthcare GmbH, Erlangen, Germany

6 Cardiac Surgery Department, IRCCS Policlinico San Donato, San Donato Milanese, Italy

MV	Mitral Valve
PCA	Principal Component Analysis
SD	Standard Deviation
SV	Stroke Volume
TE	Echo Time
TR	Repetition Time
V	Volume
VR	Vortex Ring
W	Vorticity

1 Background

Ischemic cardiomyopathy (ICM) is the most common type of dilated cardiopathy that affects the left ventricle (LV). It is characterized by myocardial scarring and progressive chamber enlargement, resulting from an adverse remodelling process. As a result, the LV loses its ellipsoid shape and becomes more spherical, leading to impaired ventricular function [1, 2]. The scarred LV wall segments lose contractility and become akinetic or hypokinetic. Additionally, nonischemic wall regions, known as remote myocardium, can also experience dysfunction due to excessive wall stress [3].

Although it is clear that a consequence of myocardial infarction is LV systolic dysfunction due to myocardial loss, it remains unclear why some patients can develop diastolic dysfunction at an early stage, regardless of age and LV ejection fraction (EF) [4]. In a previous study on ICM patients with previous anterior myocardial infarction, the intracavitary blood flow during diastole showed a reduction of blood kinetic energy (KE) and intracavitary hemodynamic force, possibly associated with an increased amount of blood stagnation and with the loss of LV wall contractility, respectively [5]. In a series of patients with myocardial infarction and preserved EF, Krauter et al. reported alterations in the shape of the 3D vortex ring (VR) during early diastole. The VR is generated at the tips of the mitral valve (MV) leaflets and encloses the inflow jet during LV diastolic filling [6]. This finding is noteworthy, as previous studies have suggested that the diastolic VR supports ventricular filling by storing part of the KE of the entering flow into its rotary motion. This, in turn, helps in directing blood flow towards the aorta in the following systole [7]. Furthermore, alterations in diastolic VR have been observed in various types of LV dysfunction [6, 8–10] and can reflect subtle or temporary changes in LV function. Therefore, quantifying and characterizing VR parameter could provide a more comprehensive understanding of LV diastolic function, with a potential impact on the diagnostic process [11] and on the definition of early markers of progressive LV dysfunction [8].

Finally, ICM not only affects LV function, but also impairs the function of the left atrium (LA). LV wall stiffening associated with myocardial necrosis reduces LV diastolic compliance, leading to an increase in LA pressure, LA wall stress, and LA wall stretches [12]. This effect is correlated with the extent of the LV wall-scarred regions and mediated by the LV-LA interplay [13].

On this basis, in the present study, magnetic resonance imaging (MRI) was exploited to combine the analysis of both LA and LV function in ICM patients, also including a comparison with a cohort of healthy controls. LA function was assessed by quantifying LA volumes and strains based on cine MRI. LV diastolic function was assessed by quantifying the geometry, energetics, and spinning motion of the 3D VR using time-resolved phase-contrast MRI with three-directional velocity encoding (4D Flow MRI). Through a systematic and highly automated approach, we aimed to (i) quantify the alterations of the 3D VR geometry and energetics in ICM patients with systo-diastolic LV dysfunction as compared to healthy controls and (ii) to further investigate the atrio-ventricular coupling through the combined analysis of VR-related metrics and MRI-derived LA function in ICM patients.

2 Methods

2.1 Study population

A cohort of ICM patients ($n = 15$) and a cohort of healthy controls ($n = 15$) with comparable age and sex, no history of cardiac disease, and no cardiovascular risk factors were included in the study. The diagnosis of ICM was based on the presence of a previous anterior myocardial infarction, LV dilation, and systolic dysfunction. Systolic dysfunction was assessed using 2D echocardiography and MRI, and it was defined by a LV EF below 49% [14], while diastolic dysfunction was assessed using 2D echocardiography (Table S1) [15]. Patients with more than mild aortic or mitral valvulopathy were excluded. The study conformed to the Ethical Guidelines of the Declaration of Helsinki; all subjects provided written informed consent.

2.2 MRI acquisitions and image analysis

All subjects underwent MRI acquisition at 1.5 T using a MAGNETOM Aera (Siemens Healthcare, Erlangen, Germany) scanner. A balanced steady-state free precession (bSSFP) cine sequence with retrospective ECG gating

was used to acquire short- and long-axis LV views. The following image parameters were considered: TE (Echo Time) = 1.1–1.8 ms, TR (Repetition Time) = 2.9–5.1 ms, flip angle = 53°–70°, slice thickness = 8 mm (no gap), pixel spacing = 1.3–1.8 mm, and reconstructed temporal resolution = 24.3–40.6 ms (reconstructed phases = 30).

In the same session, 4D Flow MRI data were acquired using a time-resolved 3D gradient echo research sequence with three-directional velocity encoding. 4D Flow MRI data were acquired with a para-sagittal field of view covering the entire LV and during free-breathing, with retrospective ECG triggering and adaptive respiratory gating. Sequence parameters were as follows: velocity encoding = 80–150 cm/s to limit aliasing, flip angle = 7° (without contrast agent)–15° (with contrast agent), TE = 2.3–2.6 ms, TR = 4.8–5.2 ms, voxel size = $(2.0 - 2.9) \times (2.0 - 2.9) \times (2.0 - 2.8)$ mm^3, reconstructed temporal resolution = 24.5–47.3 ms (reconstructed phases = 30). 4D Flow MRI data were corrected for eddy currents [16] and aliasing [17], if present; a $3 \times 3 \times 3$ median filtering was also applied to reduce noise. All patients were in sinus rhythm during MRI acquisition.

2.3 LA analysis

LA endocardial borders were manually traced in 2- and 4-chamber views to obtain the LA volume, through the biplane area-length method [18]. LA V^{max} and LA V^{min} were obtained at the timeframe before the MV opening and in the timeframe corresponding to the MV closure, respectively. LA $V^{\mathrm{pre\,A}}$ was obtained at the timeframe immediately before the atrial contraction. LA EF (total, passive, active) was computed as follows:

$$
\begin{aligned}
\mathrm{LAEF} &= \frac{\mathrm{LA}V^{\mathrm{max}} - \mathrm{LA}V^{\mathrm{min}}}{\mathrm{LA}V^{\mathrm{max}}} \cdot 100 \\
\mathrm{LAEF}_{\mathrm{passive}} &= \frac{\mathrm{LA}V^{\mathrm{max}} - \mathrm{LA}V^{\mathrm{preA}}}{\mathrm{LA}V^{\mathrm{max}}} \cdot 100 \quad [\%] \\
\mathrm{LAEF}_{\mathrm{active}} &= \frac{\mathrm{LA}V^{\mathrm{preA}} - \mathrm{LA}V^{\mathrm{min}}}{\mathrm{LA}V^{\mathrm{preA}}} \cdot 100
\end{aligned}
\tag{1}
$$

LA strain (ε) analysis was performed using cardiac MRI feature-tracking on a dedicated software (Qstrain, version 2.1.12.2, Medis Medical Imaging Systems, Leiden, The Netherlands). LA endocardial borders were manually traced in 2- and 4-chamber views, and the automated tracking algorithm was applied, with manual correction for minor misalignments. The three LA phasic functions (reservoir, conduit, and booster pump) were analyzed (Figure S1).

2.4 LV analysis: global features and chamber segmentation

LV volumes, mass, and EF were calculated from bSSFP cine images using a thresholding method in Medis (Qmass

MR version 6.2.1, Medis Medical Imaging Systems). The shape of the LV was described through the LV diastolic sphericity index (DSI) obtained from the ratio between the LV end-diastolic volume (EDV) and the volume of an ideal sphere with the LV long-axis as diameter. The LV long-axis was computed as the mean value of the measurements obtained from 2-chamber and 4-chamber views [19, 20]. The LV global functionality index (LVGFI) was computed as reported in [21]. In ICM patients, late gadolinium enhancement (LGE) was quantified in grams by manual endocardial and epicardial contouring, and subsequent use of the standard deviation (SD) method with a ≥ 5 SD from remote myocardium was considered as LGE [22]. Manual adjustments were adopted in case of disagreement on visual assessment for the remote area automatically identified by the software. LGE is reported as percentage of total myocardial mass.

2.5 LV analysis: identification of E-wave and A-wave

bSSFP cine images were segmented to reconstruct dynamic LV masks as in [5, 23]. The dynamic LV masks were registered in space and time over the 4D Flow MRI data to extract the voxels corresponding to the LV chamber at every timeframe.

At each timeframe, blood KE, i.e., the energy that a volume of blood possesses due to its motion, was computed for the whole LV chamber, yielding KE$_{\mathrm{LV}}$. In general, KE was computed as follows [24]:

$$
\mathrm{KE} = \sum_{i=1}^{N} \frac{1}{2} \rho V_{\mathrm{voxel}} |\boldsymbol{v}_i|^2 [\mathrm{mJ}]
\tag{2}
$$

where ρ is the blood density (equal to 1025 kg/m^3), V_{voxel} is the voxel volume, $|\boldsymbol{v}|$ is the velocity magnitude, and N is the total number of voxels within the region of interest.

Peak E-wave and peak A-wave, associated with early rapid filling and atrial contraction, respectively, were determined by identifying two distinct peaks in the time course of KE$_{\mathrm{LV}}$ during the diastolic phase (Figure S2).

2.6 LV analysis: vortex ring detection

At peak E-wave and at peak A-wave, intraventricular VRs were detected using the λ_2 method [25–27], which is a widely accepted technique for vortex detection [28] and identifies 3D VR based on the gradient of blood velocity field. The velocity gradient tensor $\boldsymbol{L}$ was computed at each voxel as follows:

$$
\boldsymbol{L} = \begin{bmatrix} \frac{\partial v_x}{\partial x} & \frac{\partial v_x}{\partial y} & \frac{\partial v_x}{\partial z} \\ \frac{\partial v_y}{\partial x} & \frac{\partial v_y}{\partial y} & \frac{\partial v_y}{\partial z} \\ \frac{\partial v_z}{\partial x} & \frac{\partial v_z}{\partial y} & \frac{\partial v_z}{\partial z} \end{bmatrix}
\tag{3}
$$

where v_x, v_y, and v_z are the three velocity components of the velocity vector field acquired through 4D Flow MRI in the three spatial dimensions x, y, and z. To compute space derivatives of velocity, a weighted central difference scheme was employed, due to the nearly isotropic space resolution of 4D Flow MRI data [29, 30]. The resulting velocity gradient tensor L was then decomposed into its symmetric part S (i.e., strain deformation tensor) and the antisymmetric part $\boldsymbol{\Omega}$ (i.e., spin tensor):

$$S = \frac{L + L^T}{2} \tag{4}$$

$$\boldsymbol{\Omega} = \frac{L - L^T}{2} \tag{5}$$

To identify the voxels belonging to VR, the three largest eigenvalues were computed for $S^2 + \boldsymbol{\Omega}^2$ and then sorted from largest to smallest ($\lambda_1 \geq \lambda_2 \geq \lambda_3$). Ideally, a voxel would be classified as part of the vortex ring if $\lambda_2 < 0$. However, since velocity data obtained from 4D Flow MRI are affected by noise, a more robust threshold value ($T_{\lambda 2}$) was defined to identify the voxels in the vortex structure as those with $\lambda_2 < T_{\lambda 2}$. $T_{\lambda 2}$ was defined as follows:

$$T_{\lambda_2} = K\mu \tag{6}$$

where μ is the λ_2 average of voxels with $\lambda_2 < 0$ and K is a real number (with $K > 1$). For each analyzed subject, at both peak E-wave and peak A-wave, K was set through a semi-automatic procedure, which minimized the presence of attached trailing structures while preserving the toroidal shape of the vortex ring when present [25, 31]. Based on an automatically identified reference value, K was manually fine-tuned within a narrow range of values (see Supplementary Material, Figures S3-S5).

Once the voxels associated with $\lambda_2 < T_{\lambda_2}$ were identified, the vortex ring was defined as the largest connected region of these voxels.

2.7 LV analysis: vortex ring characterization

At peak E-wave and at peak A-wave, the geometry, the energetics, and the vorticity of the diastolic VRs were quantified.

Geometry quantification The VR shape was classified as torus-shape, U-shape, or bracket-shape [6] (Figure S6). The extent of the VR was quantified as the ratio between its volume and the LV volume (V_{VR}/V_{LV}). To assess the VR circularity, the coordinates of the voxel centers corresponding to the VR were extracted to generate a point cloud. Principal component analysis (PCA) [32] was performed on the point cloud data to identify the first two
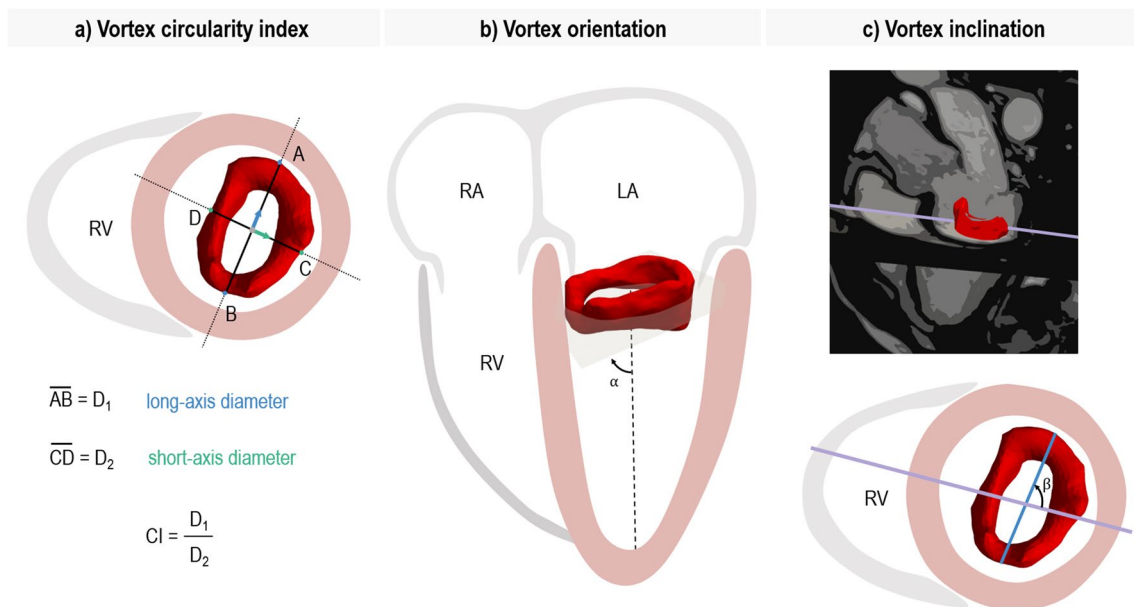
Fig. 1 Graphical representation of vortex ring geometric parameters. **a**) The vortex ring long (D_1, blue) and short (D_2, green) diameters are extracted through principal component analysis. Their ratio gives the circularity index (CI), which indicates the extent to which the VR resembles a circular shape. **b**) The orientation angle relative to the LV long-axis (α) is measured as the angle between the LV long-axis and the fitting plane of the vortex ring. An angle of 90° indicates that the vortex ring plane is perpendicular to the LV long-axis. **c**) The vortex inclination (β) is defined as the angle between the vortex ring long-axis diameter and the intersection between the three-chamber LV view and the LV short-axis section that includes the VR (purple line). LA, left atrium; RA, right atrium; RV, right ventricle

principal directions. The long- (D_1) and short-axis (D_2) of the VR were identified as the VR dimensions along the first and second principal directions, respectively (Fig. 1a). The circularity index (CI) was computed as the ratio between D_1 and D_2. The VR orientation relative to LV long-axis (α) was determined as the angle between the LV long-axis (i.e., the axis perpendicular to the short-axis acquired stack) and the plane defined by the first two eigenvectors obtained from PCA (Fig. 1b). Lastly, to assess the VR inclination with respect to the LV outflow tract direction, the angle (β) between the VR long-axis and the intersection between the three-chamber LV view and the LV short-axis section that includes the VR was computed (Fig. 1c).

Energetics quantification To quantify the contribution of the vortex ring to blood KE, KE was computed through Eq. 2 over the region corresponding to the VR, yielding KE_{VR}, and the ratio KE_{VR}/KE_{LV} was obtained. Also, the ratio between KE_{VR} and V_{VR} was computed (KE_{VR}/V_{VR}).

To quantify the dissipative effects related to the vortex ring, the rate of viscous energy loss ($\dot{EL}$) was computed over the whole LV chamber ($\dot{EL}_{LV}$) and over the vortex ring ($\dot{EL}_{VR}$), based on the formula:

$$\dot{EL} = \mu \sum_{i=1}^{N} \phi_{v,i} V_{voxel} \quad [mW] \tag{7}$$

where μ is blood viscosity (set equal to 3.7 cP) and $\phi_{v,i}$ is the viscous dissipation function per unit volume. ϕ_v was computed from the Navier–Stokes energy equation:

$$\phi_v = 2\left[\left(\frac{\partial v_x}{\partial x}\right)^2 + \left(\frac{\partial v_y}{\partial y}\right)^2 + \left(\frac{\partial v_z}{\partial z}\right)^2 - \frac{1}{3}(\nabla \bullet v)^2\right]$$
$$+ \left(\frac{\partial v_y}{\partial x} + \frac{\partial v_x}{\partial y}\right)^2 + \left(\frac{\partial v_z}{\partial y} + \frac{\partial v_y}{\partial z}\right)^2 + \left(\frac{\partial v_x}{\partial z} + \frac{\partial v_z}{\partial x}\right)^2 \quad \left[\frac{1}{s}\right] \tag{8}$$

where $\nabla \bullet v$ is the divergence of the velocity field [33]. The ratio $\dot{EL}_{VR}/\dot{EL}_{LV}$ was computed.

Vorticity quantification To quantify the contribution of the vortex ring to blood spinning motion, the instantaneous integral vorticity magnitude was computed for VR (W_{VR}) and for the whole LV chamber (W_{LV}), as follows [34–36]:

$$W = \sum_{i=1}^{N} |\boldsymbol{\omega}_i| V_{voxel} \quad \left[\frac{ml}{s}\right] \tag{9}$$

where, at the ith voxel, $|\boldsymbol{\omega}|$ is the magnitude of the vorticity vector $\boldsymbol{\omega}$ defined as follows:

$$\boldsymbol{\omega} = \left(\frac{\partial v_z}{\partial y} - \frac{\partial v_y}{\partial z}, \frac{\partial v_x}{\partial z} - \frac{\partial v_z}{\partial x}, \frac{\partial v_y}{\partial x} - \frac{\partial v_x}{\partial y}\right) \quad \left[\frac{1}{s}\right] \tag{10}$$

The ratio W_{VR}/W_{LV} was computed.

2.8 Intra- and inter-observer reproducibility analysis

Because the setting of the value of the K parameter impacts each subsequent calculation, the following reproducibility analysis was performed at peak E-wave and at peak A-wave on each dataset: two double-blinded operators set the value of K completely manually; one of them repeated the setting after 3 months; finally, both operators repeated the setting of K through the semi-automated approach. For every setting of K, α, CI, and V_{VR} were computed for the vortex ring.

The analysis allowed to assess by how much the semi-automatic approach reduced inter-operator variability as compared to intra- and inter-operator variability of the fully manual approach.

2.9 Statistical analysis

Continuous variables were expressed as mean $\pm$ SD, if normally distributed, and as median (IQR) otherwise. Normality of the distribution of continuous data was tested through the Shapiro–Wilk test, and differences between controls and ICM were computed through unpaired t-test, if normally distributed, or through Mann–Whitney otherwise. Fisher's test was used to test sex distribution between groups. Also, the Pearson correlation coefficient (r) was used to measure the strength of association between the

Table 1 Demographic, morphological, and functional characteristics of the left ventricle

	Healthy controls ($n=15$)	ICM ($n=15$)	p
Age (years)	61 ± 7	65 ± 10	0.29
BSA (m^2)	1.9 ± 0.2	1.8 ± 0.2	0.41
Sex (F, %)	4 (33)	1 (8)	> 0.99
Heart rate (bpm)	65 ± 8	68 ± 9	0.35
LV EDV$_i$ (ml/m^2)	69 ± 10	120 ± 27	< 0.0001
LV ESV$_i$ (ml/m^2)	22 ± 5	82 ± 28	< 0.0001
LV SV$_i$ (ml/m^2)	47 ± 7	38 ± 9	0.005
LV EF (%)	68 ± 4	32 ± 9	< 0.0001
LV mass$_i$ (g/m^2)	62 ± 8	95 ± 19	< 0.0001
LV DSI (-)	0.36 ± 0.05	0.46 ± 0.10	0.001
LVGFI (%)	44.7 ± 4.0	20.4 ± 6.4	< 0.0001
Necrotic percentage (%)	-	22.9 ± 7.5	-

Data are expressed as mean $\pm$ SD, if normally distributed, and as median (IQR) otherwise. *ICM*, ischemic cardiomyopathy; *BSA*, body surface area; bpm, beats per minute; *LV*, left ventricle; *EDV*, end diastolic volume; *ESV*, end systolic volume; *SV*, stroke volume; *EF*, ejection fraction; *DSI*, diastolic sphericity index; *LVGFI*, left ventricle global functionality index

Table 2 Morphological and functional characteristics of the left atrium

	Healthy controls ($n = 15$)	ICM ($n = 15$)	p
LA V^{max}_i (ml/m^2)	36 ± 11	45 ± 23	0.192
LA V^{min}_i (ml/m^2)	14 ± 7	24 (13; 37)	0.021
LA V^{preA}_i (ml/m^2)	26 ± 10	38 ± 21	0.051
LA EF (%)	62 ± 10	44 (38; 59)	< 0.0001
LA EF$_{passive}$ (%)	29 ± 9	17 ± 9	0.001
LA EF$_{active}$ (%)	47 ± 11	32 (24; 40)	0.002
ε_s (%)	37.0 ± 16.5	17.7 ± 7.0	0.0003
ε_e (%)	15.9 ± 7.9	7.1 ± 4.6	0.0009
ε_a (%)	21.1 ± 9.9	10.5 ± 5.0	0.001

Data are expressed as mean $\pm$ SD, if normally distributed, and as median (IQR) otherwise. *ICM*, ischemic cardiomyopathy; *LA*, left atrium; *EF*, ejection fraction; ε_s, strain reservoir; ε_e, strain conduit; ε_a, strain booster

variables extracted for the control group and for the ICM group. Linear regression and Bland–Altman analyses were used to assess intra- and inter-observer reproducibility.

Statistical analyses were performed with GraphPad Prism 8 (GraphPad Software Inc., La Jolla, CA, USA); a p-value < 0.05 was considered significant.

3 Results

The demographic, morphological, and functional characteristics of the two groups are detailed in Tables 1 and 2. The two groups were comparable in terms of age, body surface area, and sex distribution. ICM patients had significantly higher LV volumes, LV mass and LV DSI, lower LV stroke volume (SV), LV EF, and LVGFI, as well as significantly reduced LA V^{min}_i, LA EF, and LA strain.

3.1 Qualitative assessment *of vortex* ring

The λ_2 algorithm detected VRs at both E- and A-wave peak frames for all the analyzed subjects (Figs. 2, 3; Video S1, and S2), but one ICM patient did not develop a vortex at peak E-wave. Thirty-five out of the 59 detected VRs were torus-shaped: in 11 controls and 6 ICM patients at peak E-wave and in 9 healthy controls and 9 ICM patients at peak A wave. The remaining VRs were U-shaped.

3.2 Characterization *of vortex* rings

Geometry quantification CI and vortex angles (α and β) were quantified for the entire population (Table 3; Figs. 2, 3). At peak E-wave, statistically significant differences

were found between ICM patients and healthy controls in terms of both CI and vortex angles: in ICM patients, D_1 was larger (45.9 ± 6.1 mm vs. 41.5 ± 4.6 mm in healthy controls; $p = 0.03$), and the CI deviated more from 1 (1.5 ± 0.4 vs. 1.3 ± 0.2 in controls; $p = 0.032$). In ICM patients, the vortex orientation α ranged from 23 to 78°, while it ranged from 62 to 85° in healthy controls ($p = 0.003$). Ring overturning, i.e., $\alpha > 90°$ indicating a completely tilted orientation of the ring, was never observed. In ICM patients, the vortex inclination angle β ranged between 85 and 161°, while it ranged between 56 and 117° for healthy controls ($p = 0.002$).

At peak A-wave, in ICM patients, D_1 was larger (50.6 ± 6.0 mm vs. 46.1 ± 5.5 in controls; $p = 0.04$) and CI deviated more from 1 (1.7 ± 0.4 vs. 1.4 ± 0.2 in controls, $p = 0.034$). α ranged from 52 to 78° in ICM patients and from 61 to 82° in healthy controls ($p = 0.016$). Ring overturning was never observed. In ICM patients, the vortex inclination angle β ranged between 84 and 152°, while for healthy controls, it ranged from 70 to 110° ($p = 0.036$).

Energetics, vorticity, and volume quantification Both at peak E-wave and peak A-wave, EL_{VR}/EL_{LV}, W_{VR}/W_{LV}, V_{VR}/V_{LV}, and KE_{VR}/V_{VR} significantly decreased in ICM patients vs. healthy controls, while V_{VR} remained comparable between normal and pathologic conditions.

3.3 Vortex ring parameters association with LV and LA morphology and function

For healthy controls, at peak E-wave, V_{VR} reported a strong correlation with LV EDV$_i$ ($r = 0.74$, $p = 0.002$) and LV ESV$_i$ ($r = 0.67$, $p = 0.006$). KE_{VR}/KE_{LV} reported moderate correlation with LA EF$_{active}$ ($r = 0.58$, $p = 0.025$). α showed moderate correlation with LA EF$_{passive}$ ($r = 0.58$, $p = 0.022$). At peak A-wave, V_{VR}/V_{LV} reported moderate correlation with LA EF$_{active}$ ($r = 0.60$, $p = 0.014$).

For ICM patients at peak E-wave, α reported very strong correlation with LV EDV$_i$ ($r = -0.84$, $p = 0.0002$), LV ESV$_i$ ($r = -0.89$; $p < 0.0001$), strong correlation with LV EF ($r = 0.73$; $p = 0.003$), LVGFI ($r = 0.70$; $p = 0.006$), and LV mass$_i$ ($r = -0.65$; $p = 0.011$) (Fig. 4).

CI showed moderate correlation with LV EDV$_i$ ($r = 0.58$, $p = 0.030$) and LV ESV$_i$ ($r = 0.60$; $p = 0.024$) and strong correlation with LA EF$_{passive}$ ($r = -0.69$, $p = 0.006$). V_{VR}/V_{LV} reported moderate correlation with LV EDV$_i$ ($r = -0.59$, $p = 0.027$) and LV ESV$_i$ ($r = -0.55$; $p = 0.041$). KE_{VR}/V_{VR} showed moderate correlation with the necrotic mass expressed as percentage ($r = -0.54$, $p = 0.042$). At peak A-wave, CI reported strong correlation with LV mass$_i$ ($r = 0.73$, $p = 0.002$), and KE_{VR}/V_{VR} showed strong correlation with LV mass$_i$ ($r = 0.73$, $p = 0.002$).

Fig. 2 Diastolic vortex rings in a healthy control. Example of vortex ring during early filling (to the left) and late filling (to the right), for one healthy control in a short-axis view (at the top) and in a horizontal long-axis view (at the bottom). In the short-axis view, the long- and short-axis diameters of the vortex ring are displayed for CI computation, together with the angle β. In the long-axis view (i.e., horizontal long axis displaying the four heart chambers), the angle α is displayed and streamlines show blood flow direction during the two elective diastolic timeframes. A, peak A-wave; CI, circularity index; E, peak E-wave; KE, kinetic energy; LA, left atrium; LV, left ventricle; RA, right atrium; RV, right ventricle
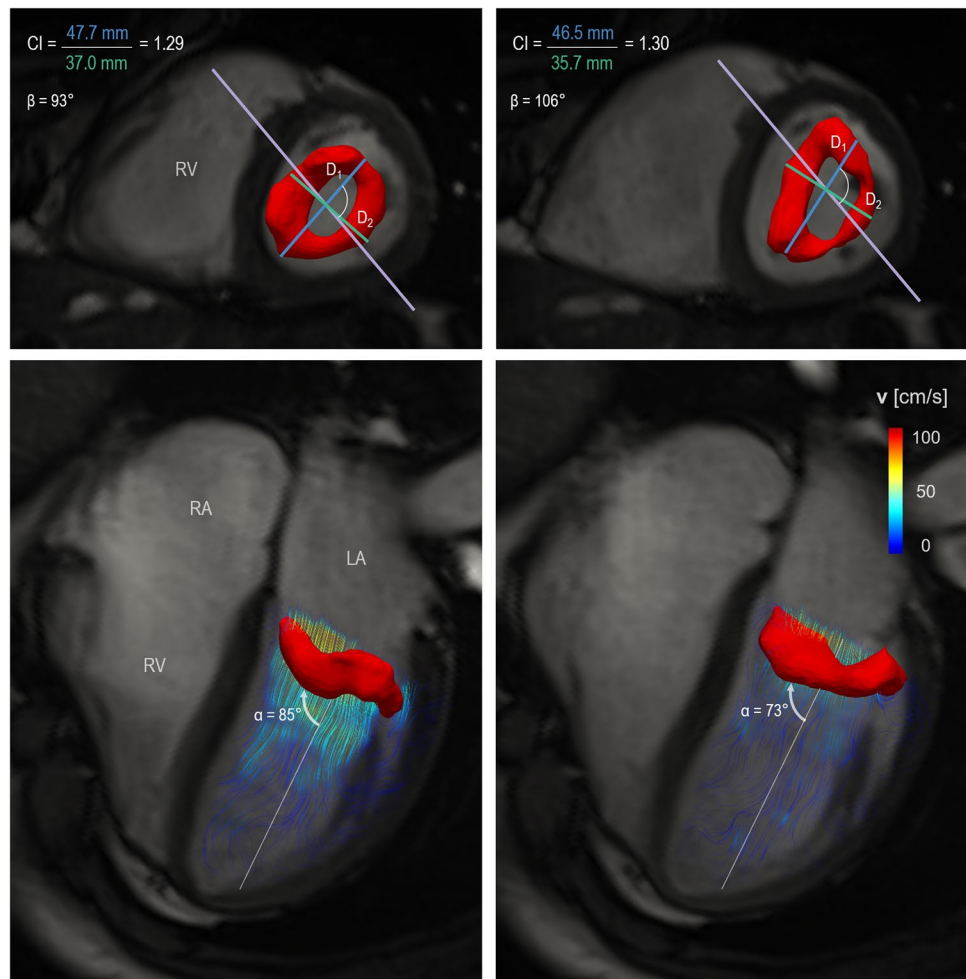
3.4 Intra- and inter-observer reproducibility

When the value of K was set through a fully manual approach, intra-observer analysis showed $r \geq 0.91$ (all $p < 0.0001$) and Bland–Altman plots exhibited a bias ranging between -1.1 and 0.26 (Figure S8); inter-observer analysis showed $r \geq 0.92$ (all $p < 0.0001$), and Bland–Altman plots exhibited a bias ranging between -1.6 and -0.4 (Figure S9). When the value of K was set through the semi-automatic method, inter-observer analysis yielded $r \geq 0.94$ (all $p < 0.0001$) and Bland–Altman plots exhibited a bias ranging between -0.01 and 0.5 (Fig. 5).

4 Discussion

This study introduced a standardized extraction method and an automatic quantitative characterization of 3D VRs during early and late diastolic LV filling in healthy controls and ICM patients. The extracted VR parameters confirmed alterations associated with pathological conditions and showed a moderate/strong correlation with concomitant alterations in LV global morphology and function, as assessed by EDV_i, ESV_i, EF, LV mass$_i$, and LVGFI, and moderate correlation with LA function, as assessed by LA $EF_{passive}$.

4.1 Methodological novelties: vortex ring extraction and analysis

The proposed λ_2 method successfully extracted vortex rings in both healthy controls and ICM patients, despite the different LV morphology and function characterizing the two groups. This result confirms the general validity of the method, as previously reported [10, 25, 31]. Of note, the novel semi-automatic method introduced in this study improved the standardization of the K parameter setting, and hence of the subsequent calculations, as it leaves minimal room for user-dependent choices.

Two of the extracted geometric parameters, namely CI and α, have already been computed in previous studies [6, 10, 31]. Elbaz et al. defined CI as the ratio between the vortex's short to long diameters: these were defined by positioning two planes on through-plane velocity encoded MR images at the annulus level and 1 cm distal of the annulus. The resulting cross-sectional images were used

Fig. 3 Diastolic vortex rings in an ICM patient. Example of vortex ring during early filling (to the left) and late filling (to the right), for one ICM patient in a short-axis view (at the top) and in a horizontal long-axis view (at the bottom). In the short-axis view, the long- and short-axis diameters of the vortex ring are displayed for CI computation, together with the angle β. In the long-axis view (i.e., horizontal long axis displaying the four heart chambers), the angle α is displayed and streamlines show blood flow direction during the two elective diastolic timeframes. The ICM patient presents aneurysmal remodelling of the apex, with a thrombus adhered to the wall. A, peak A-wave; CI, circularity index; E, peak E-wave; KE, kinetic energy; LA, left atrium; LV, left ventricle; RA, right atrium; RV, right ventricle
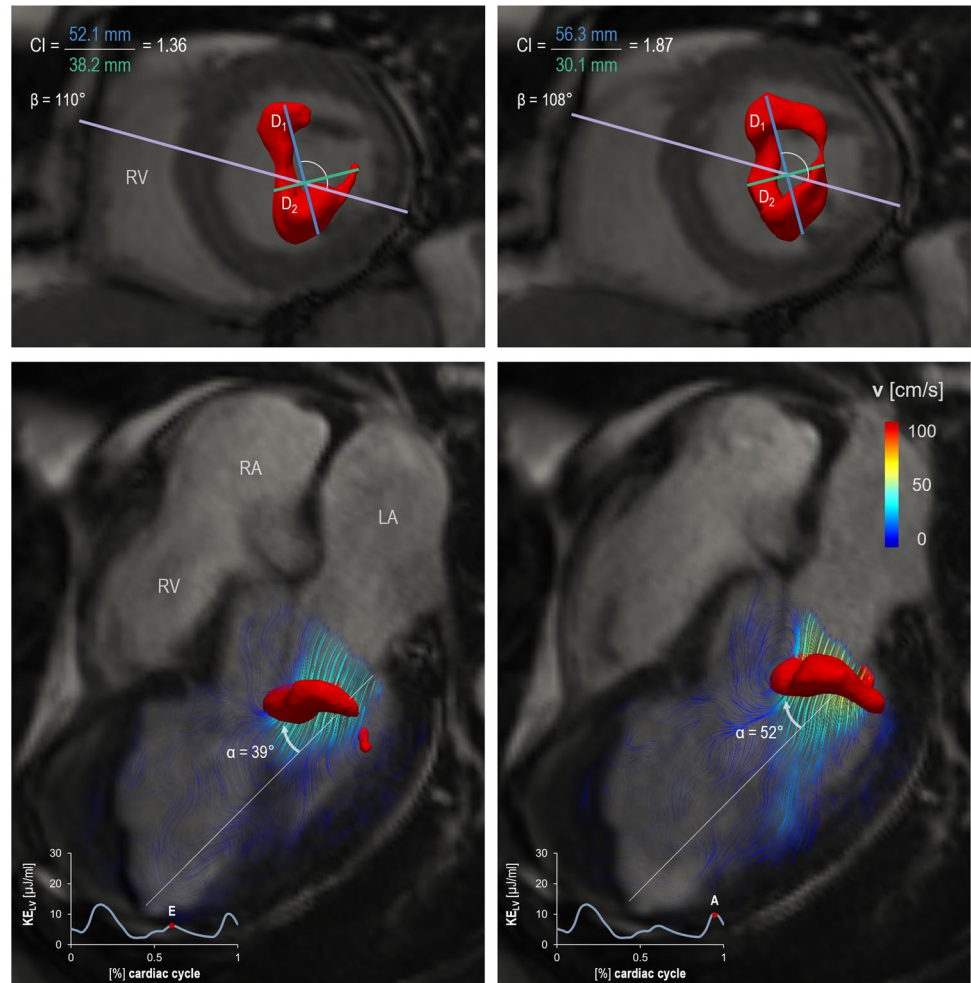
to outline the flow through the MV and to define the diameters [31]. Kräuter et al. defined the long-axis diameter as the largest principal axis length of an ellipsoid fitted to the vortex ring and the short-axis as the second largest principal axis length [6]. In the present study, PCA stands out from previously implemented approaches due to its high level of automation in the definition of D_1 and D_2. Unlike the other methods, which required manual tracing or shape fitting, PCA reduced operator dependency and analysis time expense.

The computation of the vortex inclination angle β was introduced to assess the orientation of the VR relative to the LV outflow tract, as VRs help redirecting the MV inflow towards the aorta [8, 37]. The angle β was automatically computed, using the VR long-axis diameter defined using PCA and the intersection between the three-chamber LV view and LV short-axis section, defined anatomically during MR acquisition.

Vorticity and KE were evaluated at VR level in [6]: the maximum and mean vorticity were determined in the vortex region, while KE was evaluated in the VR and

normalized by the VR volume (i.e., KE_{VR}/V_{VR}). However, this is the first study introducing the quantification of ratios between VR and LV parameters (i.e., KE_{VR}/KE_{LV}, EL_{VR}/EL_{LV}, W_{VR}/W_{LV} and V_{VR}/V_{LV}) for the characterization of VR in healthy and pathologic conditions and investigating the influence of the LA function on vortex formation.

4.2 Vortex ring parameters in controls and ICM patients

In healthy controls, α and CI values extracted at peak E-wave and at peak-A wave were within the previously published normal range, although computed with a different method [10, 31]. In fact, in the physiological heart, adequate suction, correct MV leaflets shape, and normal LV wall compliance generate complex flow patterns during LV filling, leading to rotational fluid motion near the MV leaflets and to VR formation [38]. The vortex ring forms at the tip of the MV, with the septal side positioned towards the apex (i.e., $\alpha < 90°$), owing to the asymmetrical shape of the MV leaflets (i.e.,

Table 3 Study population vortex ring characteristics

		Healthy controls ($n=15$)	ICM ($n=15$)	p-value
Peak E	α (°)	73.9 ± 6.8	59.7 ± 15.1	0.003
	β (°)	87.7 ± 19.8	113.7 ± 20.2	0.002
	CI $(-)$	1.3 ± 0.2	1.5 ± 0.4	0.032
	$KE_{VR}/KE_{LV}(-)$	0.34 ± 0.13	0.20 ± 0.13	0.008
	$\dot{EL}_{VR}/\dot{EL}_{LV}(-)$	0.22 (0.19; 0.27)	0.10 ± 0.05	<0.0001
	$W_{VR}/W_{LV}(-)$	0.28 (0.25; 0.35)	0.15 ± 0.07	<0.0001
	$V_{VR}/V_{LV}(-)$	0.12 ± 0.03	0.06 ± 0.03	<0.0001
	KE_{VR}/V_{VR}(mJ/ml)	0.08 ± 0.04	0.04 ± 0.03	0.008
	V_{VR}(ml)	11.0 ± 3.3	11.5 ± 5.3	0.764
Peak A	α (°)	70.7 ± 6.2	63.2 ± 9.4	0.016
	β (°)	98.0 ± 11.7	110.0 ± 17.6	0.036
	CI (-)	1.4 ± 0.2	1.7 ± 0.4	0.034
	$KE_{VR}/KE_{LV}(-)$	0.27 ± 0.13	0.25 ± 0.11	0.588
	$\dot{EL}_{VR}/\dot{EL}_{LV}(-)$	0.17 ± 0.07	0.11 ± 0.05	0.017
	$W_{VR}/W_{LV}(-)$	0.23 ± 0.06	0.18 ± 0.08	0.042
	$V_{VR}/V_{LV}(-)$	0.08 ± 0.02	0.06 ± 0.02	0.0032
	KE_{VR}/V_{VR}(mJ/ml)	0.05 (0.04; 0.6)	0.04 ± 0.02	0.045
	V_{VR}(ml)	10.7 ± 2.5	13.2 ± 5.1	0.110

Data are expressed as mean $\pm$ SD, if normally distributed, and as median (IQR) otherwise. ICM, ischemic cardiomyopathy; CI, circularity index; KE, kinetic energy; $\dot{EL}$, rate of viscous energy loss; V, volume; W, vorticity

longer anterior and shorter posterior) and their interaction with LV wall [37, 38]. Additionally, β illustrated that the VR long-axis is orthogonal to the LV outflow tract direction.

As highlighted by KE_{VR}/KE_{LV}, vortex KE accounts for approximately 20–30% of the total LV inflow KE, confirming its role in energy storage. Similarly, the VR extends over a relevant portion of the whole LV volume ($\sim 10\%$), supporting Dabiri's hypothesis that large VRs can efficiently transport a large amount of blood into the LV during diastole without forming a turbulent jet [39].

In ICM patients, VRs exhibited a more elliptical shape, with significantly increased CI values as compared to healthy controls. Changes in CI were associated with a disproportionate increase in the D_1 dimension, with respect to D_2. This phenomenon might be attributed to the structural alterations affecting both the infarcted anterior wall region and the remote myocardium. The reduced regional wall compliance in these areas may prevent the extension of D_2, resulting in a more elliptical VR shape, and may also lead to obtuse β angles. Of note, alterations in CI were not paired by alterations in the extent of the 3D VRs: in ICM patients, V_{VR} was similar as in healthy controls, although one may expect that in the dilated LV chamber of ICM patients, more room is available for the VR to expand, thus leading to larger vortexes. This effect may have two consequences in ICM patients: first, VRs cannot reach the LV endocardium and thus cannot prevent thrombus formation [40]; second, the blood mixing function of VRs is reduced, as evidenced by

the significant decrease found in $\dot{EL}_{VR}/\dot{EL}_{LV}$ and W_{VR}/W_{LV}, and, as highlighted in our previous study, by the increase found in the residual volume component, i.e., the portion of blood that resides within the LV for at least two cardiac cycles [5]. These conditions might increase the risk of stasis and thrombus formation [41, 42], and this is also supported by thrombus presence (ranging from small to extensive) in six ICM patients at the time of MRI.

Furthermore, α showed a significant reduction as compared to controls and reported very strong correlation with LV size (i.e., EDV_i and ESV_i). Together with the strong correlation found with LVGFI, which integrates the global LV remodelling and functional variables, this may suggest that α is sensitive to LV chamber remodelling occurring in ICM patients, with progressive LV dilation and distortion of the normal LV elliptical shape.

From the energetic standpoint, VRs in ICM maintained the same portion of KE as in healthy controls; however, they were characterized by significantly reduced KE_{VR}/V_{VR} values, and smaller values of this parameter were associated with a larger necrotic mass percentage.

4.3 Added value of 4D Flow MRI-based vortex analysis

The ICM patients considered in this study were characterized by systolic and diastolic dysfunction. These were
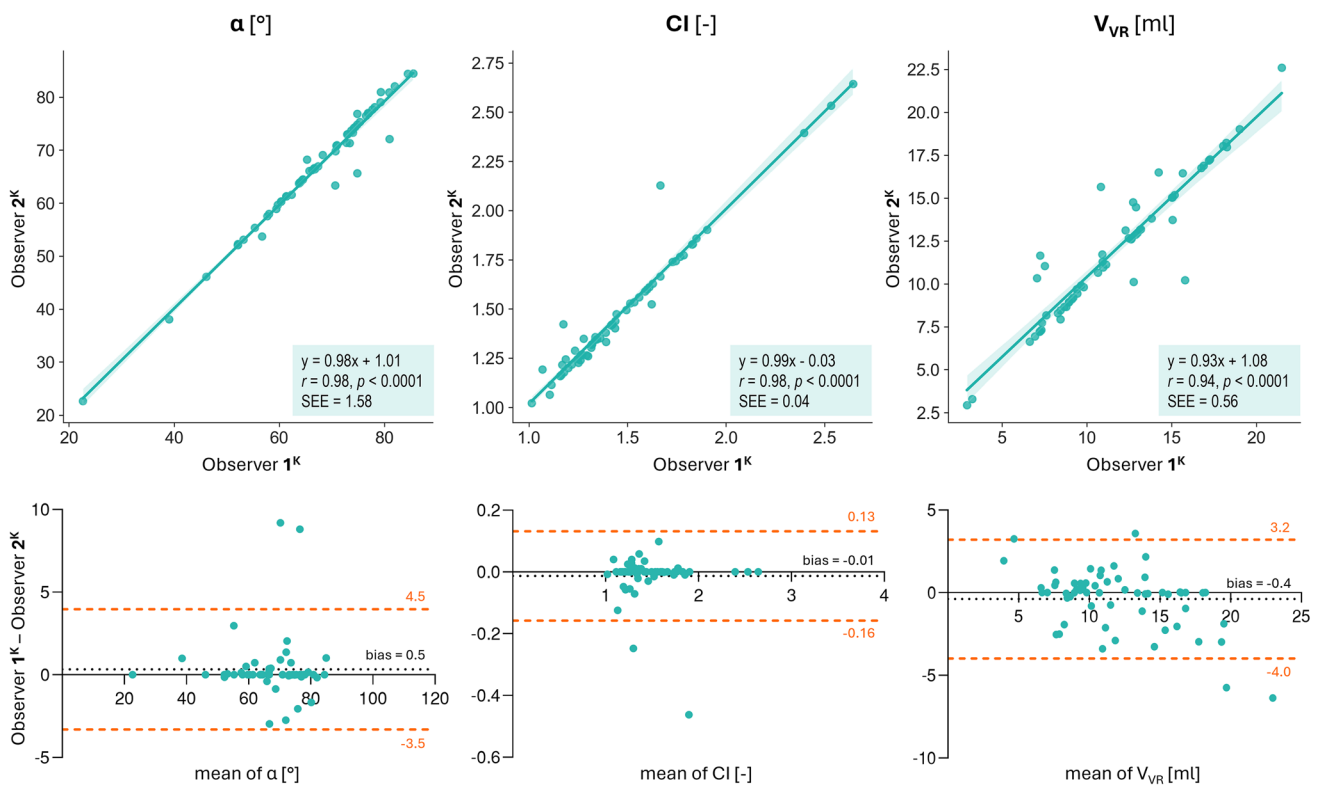
Fig. 4 Multiple linear regression plots showing the Pearson correlation between α and LV parameters (i.e., LV EDV$_i$, LV ESV$_i$, LV EF, and LVGFI) for healthy controls (orange) and ICM (purple). The plot shows the reference line (continuous line) and confidence interval at 95% (semi-transparent area). EDV, end-diastolic volume; ESV, end-systolic volume; EF, ejection fraction; LVGFI, left ventricle global functionality index
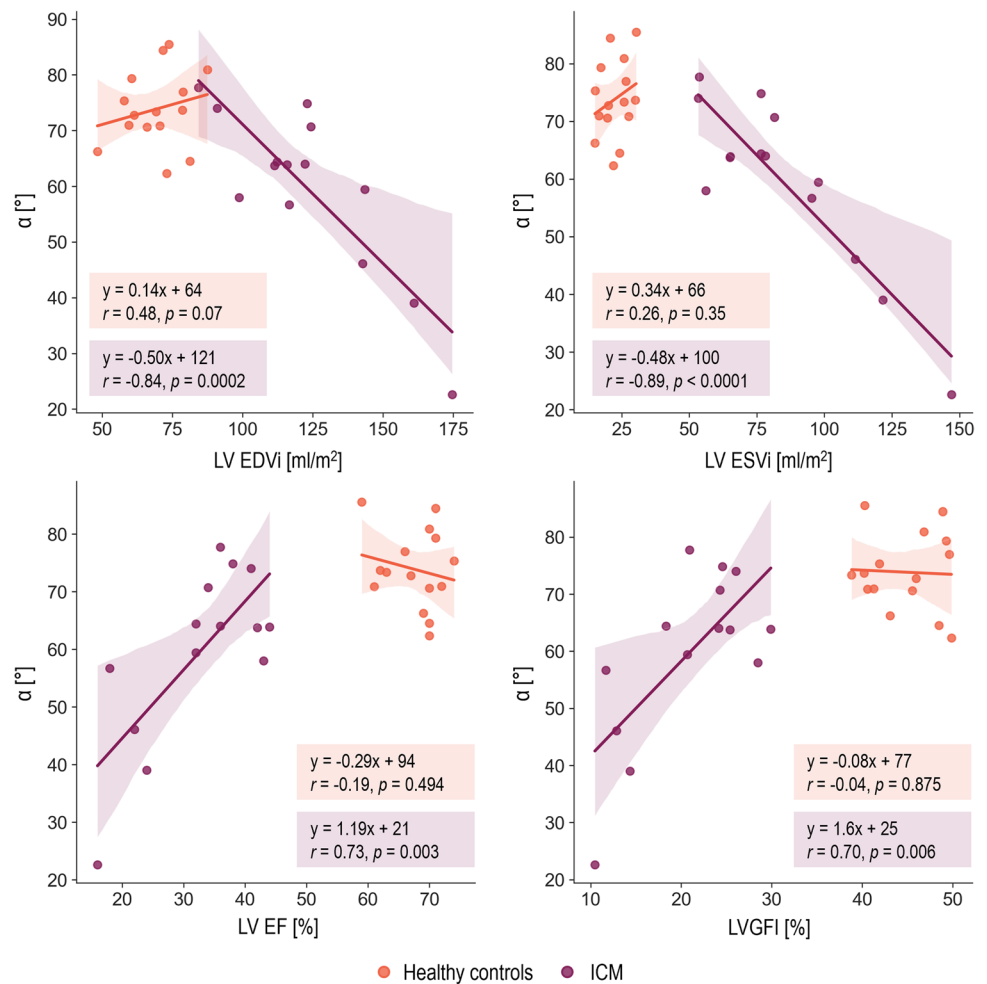
highlighted by standard MRI-derived indices of global ventricular function (EF, SV) and of global atrial function (ε_s, ε_e, ε_a), respectively. In these same ICM patients, the analysis of 4D Flow MRI data highlighted alterations in multiple features of the VR that is generated in diastole: shape, orientation, energetics, and vorticity. In particular, VR orientation was analyzed in terms of the inclination of the vortex plane with respect to the LV long-axis (α) and with respect to the LVOT direction (β). Of note, alterations in both angles were detected, but none of these angles correlated with indices of global atrial function, and only α correlated with indices of global LV systolic function. This evidence suggests a link between the orientation of the diastolic VR, and possibly its direction of propagation in the LV chamber during diastole, and LV pumping function in the subsequent systolic phase. Because blood entering the LV in diastole does not flow directly into the LVOT in systole through the shortest path, but follows a ribbon-like path from the mitral valve to the LV apex and from the latter to the LVOT, alterations in α and not in β correlate with alterations in EF and LVGFI. Exploring the link between diastolic LV fluid dynamics and LV systolic function may not have a direct application in

clinics, yet it may be used to get insight into pathophysiological mechanisms.

In terms of clinical applications, the analysis of the diastolic VR would be useful if its alterations could be used as early markers of the evolution of LV towards dysfunction, i.e., if these alterations would be present before macroscopic alterations in LV volume or shape and before the impairment of global LV function. This hypothesis is strongly suggested by studies such as the seminal work by Pedrizzetti and colleagues, which shows that intracardiac fluid dynamics can be clearly altered, in that case, because of temporary anomalies in electrical conduction, even in the absence of LV macroscopic reshaping or decrease in LV global function [8]. Testing the mentioned hypothesis is a long-term goal of our activity, and the present study is the first preliminary step in this direction; our ICM population was characterized by major alterations in LV function, volume, and shape; hence, it was not suitable to test such hypothesis, but for alterations in the VR to precede macroscopic LV alterations, a mandatory and not sufficient condition to be satisfied is that these same alterations are present when macroscopic LV alterations are already present.

Fig. 5 Top panel: Linear regression plots showing the Pearson correlation, from left to right, for α, CI, and V_{VR}, for inter-observer analysis. Observer 1^K and Observer 2^K selected K by starting from the K value detected by the semi-automatic algorithm. The plot shows the reference line (continuous line) and confidence interval at 95% (semi-transparent area). Bottom panel: Bland–Altman plots of the differences between Observer 1^K and Observer 2^K. CI, circularity index; SEE, standard error of estimate

4.4 Limitations

The study population was relatively small; therefore, our results are preliminary. To mitigate potential confounding factors related to different infarction patterns, we focused solely on ICM patients affected by anterior myocardial infarction. Therefore, our conclusions are not generalizable to other types of infarctions. Despite all patients being affected by anterior infarctions of comparable severity, they were heterogeneous in terms of LV characteristics and remodelling severity. Nevertheless, this study demonstrates the potential of 4D Flow MRI as a valuable tool for vortex ring detection and characterization in both healthy and diseased subjects.

Also, the considered ICM patients had similar heart rate values as compared to healthy controls. This was the only available parameter relevant to the hemodynamic status and clinical stability of the studied subjects. Hence, we cannot gain insight into their influence on intracavitary LV fluid dynamics, although such influence is likely based on the role of hemodynamic status and clinical stability on LV dysfunction.

At the current state of the art, there is no reference standard for MV vortex ring detection. The λ_2 method is the most accepted one [28] and was hence adopted in this study. Yet, it is known for being operator-dependent, owing to the potentially arbitrary setting of the K parameter that determines the threshold $T_{\lambda2}$. To mitigate the impact of this limitation, herein, we successfully introduced a semi-automatic method to set the value of K, which improved analysis reproducibility as compared to the case of a fully manual setting of K.

4D Flow MRI data are characterized by limited spatial and temporal resolution, which affect the computation of velocity derivatives and thus the accuracy in the computation of $\boldsymbol{L}$, $\boldsymbol{\omega}$, and EL. In the specific case of viscous dissipation, this limitation is exacerbated by the fact that the spatial resolution is only able to capture the irregularity of the velocity field, rather than the true in vivo viscous dissipation. However, the entire population was assessed with the same 4D Flow MRI sequence to allow for intergroup comparisons; hence, the observed inter-group differences remain valid.

The computation of ϕ_v was performed under the hypothesis of $\nabla \cdot \boldsymbol{v}$ equal to zero. However, as velocity measured through 4D Flow MRI contains errors, the divergence

typically deviates from zero [43]. The ex-post analysis showed that the $\nabla \cdot v$ contribution over the whole ϕ_v was always below 0.4% (see Supplementary material).

Finally, 4D Flow MRI was acquired in controls without the use of contrast agent; however, this difference with respect to acquisitions in ICM patients might affect the signal-to-noise ratio but not measured velocity and velocity fields [44].

5 Conclusions

Our comprehensive 4D Flow MRI analysis of diastolic VR parameters in ICM patients with anterior myocardial infarction revealed significant alterations as compared to healthy controls in terms of geometry, vorticity, and energetics. These changes in ICM patients may indicate an interplay between diastolic LA dysfunction and systolic LV functional derangements, potentially exacerbating the effects of the LV wall scar.

Supplementary Information The online version contains supplementary material available at https://doi.org/10.1007/s11517-024-03154-4.

Data availability The data underlying this article will be shared on reasonable request to the corresponding author.

Declarations

Ethics approval and consent to participate All participants provided written informed consent, and the study complies with the Helsinki Declaration.

Consent for publication Not applicable.

Competing interests Daniel Giese is an employee of Siemens Healthineers; all the other authors have no potential conflict of interest related to the contents of the manuscript.

References

1. Konstam MA, Kramer DG, Patel AR, Maron MS, Udelson JE (2011) Left ventricular remodeling in heart failure: current concepts in clinical significance and assessment. JACC Cardiovasc Imaging 4:98–108

2. Shah DJ, Kim HW, James O, Parker M, Wu E, Bonow RO et al (2013) Prevalence of regional myocardial thinning and relationship with myocardial scarring in patients with coronary artery disease. JAMA - J Am Med Assoc 309:909–918

3. Castelvecchio S, Frigelli M, Sturla F, Milani V, Pappalardo OA, Citarella M et al (2023) Elucidating the mechanisms underlying left ventricular function recovery in patients with ischemic heart failure undergoing surgical remodeling: a 3-dimensional ultrasound analysis. J Thorac Cardiovasc Surg 165:1418-1429.e4

4. Fantini F, Toso A, Menicanti L, Moroni F, Castelvecchio S (2021) Restrictive filling pattern in ischemic cardiomyopathy: insights after surgical ventricular restoration. J Thorac Cardiovasc Surg 161:651–660

5. Riva A, Sturla F, Pica S, Camporeale A, Tondi L, Saitta S et al (2022) Comparison of four-dimensional magnetic resonance imaging analysis of left ventricular fluid dynamics and energetics in ischemic and restrictive cardiomyopathies. J Magnetic Reson Imaging 56(4):1157–1170

6. Kräuter C, Reiter U, Reiter C, Nizhnikava V, Masana M, Schmidt A et al (2020) Automated mitral valve vortex ring extraction from 4D-flow MRI. Magn Reson Med 84:3396–3408. https://doi.org/10.1002/mrm.28361

7. Hong G-R, Pedrizzetti G, Tonti G, Li P, Wei Z, Kim JK et al (2008) Characterization and quantification of vortex flow in the human left ventricle by contrast echocardiography using vector particle image velocimetry. JACC Cardiovasc Imaging [Internet]. 1:705–717. Available from: https://linkinghub.elsevier.com/retrieve/pii/S1936878X08003641

8. Pedrizzetti G, La Canna G, Alfieri O, Tonti G (2014) The vortex—an early predictor of cardiovascular outcome? Nat Rev Cardiol [Internet]. 11:545–553. Available from: http://www.nature.com/articles/nrcardio.2014.75

9. Töger J, Kanski M, Carlsson M, Kovács SJ, Söderlind G, Arheden H et al (2012) Vortex ring formation in the left ventricle of the heart: analysis by 4D flow MRI and Lagrangian coherent structures. Ann Biomed Eng 40:2652–2662

10. Calkoen EE, Elbaz MSM, Westenberg JJM, Kroft LJM, Hazekamp MG, Roest AAW et al (2015) Altered left ventricular vortex ring formation by 4-dimensional flow magnetic resonance imaging after repair of atrioventricular septal defects. J Thorac Cardiovasc Surg [Internet]. 150:1233–1240.e1. Available from: https://linkinghub.elsevier.com/retrieve/pii/S0022522315012660

11. Kim I-C, Hong G-R, Pedrizzetti G, Shim CY, Kang S-M, Chung N (2018) Usefulness of Left ventricular vortex flow analysis for predicting clinical outcomes in patients with chronic heart failure: a quantitative vorticity imaging study using contrast echocardiography. Ultrasound Med Biol 44:1951–1959

12. Meris A, Amigoni M, Uno H, Thune JJ, Verma A, Kober L et al (2008) Left atrial remodelling in patients with myocardial infarction complicated by heart failure, left ventricular dysfunction, or both: the VALIANT Echo Study. Eur Heart J 30:56–65

13. Frigelli M, Sturla F, Milani V, Ramputi L, Citarella M, Menicanti L et al (2022) Prognostic value of left atrial strain quantification from 2D ultrasound imaging in post-ischemic heart failure patients: evidence from the REMODEL-HF study. Int J Cardiol 362:183–189

14. Ponikowski P, Voors AA, Anker SD, Bueno H, Cleland JGF, Coats AJS et al (2016) 2016 ESC Guidelines for the diagnosis and treatment of acute and chronic heart failure. Eur Heart J 37:2129–2200

15. Kim J, Yum B, Palumbo MC, Sultana R, Wright N, Das M et al (2020) Left atrial strain impairment precedes geometric remodeling as a marker of post-myocardial infarction diastolic dysfunction. JACC Cardiovasc Imaging 13:2099–2113

16. Walker PG, Cranney GB, Scheidegger MB, Waseleski G, Pohost GM, Yoganathan AP (1993) Semiautomated method for noise

reduction and background phase error correction in MR phase velocity data. J Magn Reson Imaging 3:521–530

17. Xiang Q-S (1995) Temporal phase unwrapping for cine velocity imaging. 529–534. https://doi.org/10.1002/jmri.1880050509

18. Kowallick JT, Kutty S, Edelmann F, Chiribiri A, Villa A, Steinmetz M et al (2014) Quantification of left atrial strain and strain rate using cardiovascular magnetic resonance myocardial feature tracking: a feasibility study. J Cardiovasc Magn Reson 16:60

19. Castelvecchio S, Careri G, Ambrogi F, Camporeale A, Menicanti L, Secchi F et al (2018) Myocardial scar location as detected by cardiac magnetic resonance is associated with the outcome in heart failure patients undergoing surgical ventricular reconstruction. Eur J Cardiothorac Surg 53:143–149

20. Mannaerts H, van der Heide JA, Kamp O, Stoel MG, Twisk J, Visser CA (2004) Early identification of left ventricular remodelling after myocardial infarction, assessed by transthoracic 3D echocardiography. Eur Heart J 25:680–687. https://doi.org/10.1016/j.ehj.2004.02.030

21. Mewton N, Opdahl A, Choi E-Y, Almeida ALC, Kawel N, Wu CO et al (2013) Left ventricular global function index by magnetic resonance imaging—a novel marker for assessment of cardiac performance for the prediction of cardiovascular events. Hypertension 61:770–778

22. McAlindon E, Pufulete M, Lawton C, Angelini GD, Bucciarelli-Ducci C (2015) Quantification of infarct size and myocardium at risk: evaluation of different techniques and its implications. Eur Heart J Cardiovasc Imaging 16:738–746

23. Riva A, Sturla F, Caimi A, Pica S, Milani P, Palladini G, et al. 4D Flow evaluation of blood non-Newtonian behavior in left ventricle flow analysis. J Biomech 110308. https://doi.org/10.1016/j.jbiomech.2021.110308

24. Garg P, van der Geest RJ, Swoboda PP, Crandon S, Fent GJ, Foley JRJ et al (2019) Left ventricular thrombus formation in myocardial infarction is associated with altered left ventricular blood flow energetics. Eur Heart J Cardiovasc Imaging 20:108–117

25. Elbaz MSM, Lelieveldt BPF, Westenberg JJM, van der Geest RJ (2014) Automatic extraction of the 3D left ventricular diastolic transmitral vortex ring from 3D whole-heart phase contrast MRI using Laplace-Beltrami signatures. 204–211. https://doi.org/10.1007/978-3-642-54268-8_24

26. Jeong J, Hussain F (1995) On the identification of a vortex. J Fluid Mech [Internet]. 285:69–94. https://www.cambridge.org/core/product/identifier/S0022112095000462/type/journal_article

27. von Spiczak J, Crelier G, Giese D, Kozerke S, Maintz D, Bunck AC (2015) Quantitative analysis of vortical blood flow in the thoracic aorta using 4D phase contrast MRI. PLoS ONE 10:e0139025

28. Kheradvar A, Pedrizzetti G (2012) Vortex formation in the heart. Vortex Formation in the Cardiovascular System. London: Springer London; 45–79. https://doi.org/10.1007/978-1-4471-2288-3

29. Piatti F, Pirola S, Bissell M, Nesteruk I, Sturla F, Della Corte A et al (2017) Towards the improved quantification of in vivo abnormal wall shear stresses in BAV-affected patients from 4D-flow imaging: benchmarking and application to real data. J Biomech 50:93–101. https://doi.org/10.1016/j.jbiomech.2016.11.044

30. Shih FY (2010) Image processing and pattern recognition: fundamentals and techniques. John Wiley & Sons Inc

31. Elbaz MSM, Calkoen EE, Westenberg JJM, Lelieveldt BPF, Roest AAW, van der Geest RJ (2014) Vortex flow during early and late left ventricular filling in normal subjects: quantitative characterization using retrospectively-gated 4D flow cardiovascular magnetic resonance and three-dimensional vortex core analysis.

J Cardiovasc Magnetic Res 16(1):78. https://doi.org/10.1186/s12968-014-0078-9

32. Jolliffe IT, Cadima J (2016) Principal component analysis: a review and recent developments. Phil Trans R Soc A: Mathematical, Phys Eng Sci 374:20150202

33. Elbaz MSM, van der Geest RJ, Calkoen EE, de Roos A, Lelieveldt BPF, Roest AAW et al (2017) Assessment of viscous energy loss and the association with three-dimensional vortex ring formation in left ventricular inflow: in vivo evaluation using four-dimensional flow MRI. Magn Reson Med 77:794–805

34. Kamphuis VP, Westenberg JJM, van der Palen RLF, van den Boogaard PJ, van der Geest RJ, de Roos A et al (2018) Scan–rescan reproducibility of diastolic left ventricular kinetic energy, viscous energy loss and vorticity assessment using 4D flow MRI: analysis in healthy subjects. Int J Cardiovasc Imaging 34:905–920. https://doi.org/10.1007/s10554-017-1291-z

35. Schäfer M, Browning J, Schroeder JD, Shandas R, Kheyfets VO, Buckner JK et al (2018) Vorticity is a marker of diastolic ventricular interdependency in pulmonary hypertension. Pulm Circ 6:46–54. https://doi.org/10.1086/685052

36. Fenster BE, Browning J, Schroeder JD, Schafer M, Podgorski CA, Smyser J et al (2015) Vorticity is a marker of right ventricular diastolic dysfunction. Am J Physiol-Heart and Circulatory Physiol 309:H1087-93. https://doi.org/10.1152/ajpheart.00278.2015

37. Kilner PJ, Yang GZ, Wilkest AJ, Mohladdlin RH, Firmin DN, Yacoub MH (2000) Asymmetric redirection of flow through the heart. Nature 404:759–761

38. Kheradvar A, Assadi R, Falahatpisheh A, Sengupta PP (2012) Assessment of transmitral vortex formation in patients with diastolic dysfunction. J Am Soc Echocardiography 25:220–227

39. Dabiri JO (2009) Optimal vortex formation as a unifying principle in biological propulsion. Annu Rev Fluid Mech 41:17–33

40. Arvidsson PM, Kovács SJ, Töger J, Borgquist R, Heiberg E, Carlsson M et al (2016) Vortex ring behavior provides the epigenetic blueprint for the human heart. Sci Rep 6:1–9

41. Hendabadi S, Bermejo J, Benito Y, Yotti R, Fernández-Avilés F, del Álamo JC et al (2013) Topology of blood transport in the human left ventricle by novel processing of Doppler echocardiography. Ann Biomed Eng 41:2603–2616

42. Charonko JJ, Kumar R, Stewart K, Little WC, Vlachos PP (2013) Vortices formed on the mitral valve tips aid normal left ventricular filling. Ann Biomed Eng 41:1049–1061

43. Zhang J, Brindise MC, Rothenberger S, Schnell S, Markl M, Saloner D et al (2020) 4D Flow MRI pressure estimation using velocity measurement-error-based weighted least-squares. IEEE Trans Med Imaging 39:1668–1680

44. Bock J, Frydrychowicz A, Stalder AF, Bley TA, Burkhardt H, Hennig J et al (2010) 4D phase contrast MRI at 3 T: effect of standard and blood-pool contrast agents on SNR, PC-MRA, and blood flow visualization. Magn Reson Med 63:330–8. https://doi.org/10.1002/mrm.22199

Alessandra Riva is currently a PhD candidate in Bioengineering at Politecnico di Milano. Her research activity focuses on the analysis of 4D Flow MRI data for the evaluation of intracavitary hemodynamics and energetics in cardiovascular diseases .

Lara Tondi is a cardiologist and medical intern in the Postgraduate School of Diagnostic and Interventional Radiology at Università degli Studi di Milano. Her research activity focuses on adult and pediatric cardiac MRI .

Simone Saitta is a Junior Assistant Professor at Politecnico di Milano, developing his research in the field of machine learning for medical image analysis and computational biomechanics .

Antonia Camporeale is a cardiologist in the Multimodality Cardiac Imaging Unit at IRCCS Policlinico San Donato, with research interest in myocardial and pericardial disease and a specific focus on the Anderson-Fabry disease .

Francesco Sturla is a bioengineer and full-time researcher at IRCCS Policlinico San Donato, with experience in patient-specific image-based modeling and computational analysis. He is also affiliated with Politecnico di Milano .

Daniel Giese is Application Developer at Siemens Healthcare GmbH, with large experience in cardiovascular MRI and specific interest for 4D Flow MRI technology and research .

Giandomenico Disabato is a cardiologist within the Multimodality Cardiac Imaging Unit at IRCCS Policlinico San Donato, with experience in cardiac stress MRI and specific research focus on cardiomyopathies .

Serenella Castelvecchio is Head of the Laboratory of Echocardiography and Follow-up of the Cardiac Surgery-Adult heart Area at IRCCS Policlinico San Donato, with specific interest for ischemic cardiomyopathy and cardiovascular prevention .

Lorenzo Menicanti is Head of the Department for Heart Surgery in Adults and Scientific Director of IRCCS Policlinico San Donato. He is currently the President of the Cardiological Network in Italy .

Massimo Lombardi is Head of the Multimodality Cardiac Imaging Unit at IRCCS Policlinico San Donato, with large experience and specific research interest in cardiac MRI .

Alberto Redaelli is Full Professor in Bioengineering at Politecnico di Milano and Chair of the Bioengineering Division. His research is mainly in the field of cardiovascular biomechanics and computational fluid dynamics, both experimental and computational .

Emiliano Votta is Associate Professor in Bioengineering at Politecnico di Milano. His main research activity focuses on the quantitative analysis and modeling of cardiovascular biological structures based on clinical imaging .